Enhanced Framework for Breast Cancer Detection in PET Images Using Hybrid Graph Convolutional Bidirectional LSTM and Hyperparameter Optimization

S.Tharani[1], Dr. R. Khanchana[2]

[1]Research Scholar, Department of Computer Science, Sri Ramakrishna College of Arts & Science for Women, India, vtharani1811@gmail.com
[2]Associate Professor, Department of Computer Science, Sri Ramakrishna College of Arts & Science for Women, India, khanchanacs@srcw.ac.in

Abstract: Breast Cancer Detection (BCD) through Positron Emission Tomography (PET) images remains a crucial area of study for efficient treatment planning and early diagnosis. In combining innovative techniques for Noise Reduction (NR), segmentation, Feature Extraction (FE), Feature Selection (FS), classification, and hyperparameter (HP)tuning, this research offers a thorough framework for PET scans for BCD. First, a Hyper-Averaging Filter (HAF) is applied to PET images to effectively remove noise and enhance image clarity, ensuring more accurate analysis. Subsequently, the Improved BIRCH algorithm is utilized for segmentation, enabling the delineation of regions of interest within the images. Gray-level zone length matrix (GLZLM) features are taken from the segmented regions to present comprehensive texture information, providing important information on the textural characteristics of breast tissue. In addition, to maximize the effectiveness of ensuing classification tasks, the most useful features from the extracted feature set are selected with the FS method known as the minimum redundancy maximum relevance (mRMR). For breast cancer classification, a hybrid optimized Inspection Boosted Graph Convolutional Bidirectional LSTM (long short-term memory) units (O-IBGC-BiLSTM) model is developed. This innovative architecture improves PET image spatial and temporal feature processing by combining Graph Convolutional Networks (GCN) with Bi-LSTM memory units. To enhance model performance, hyperparameter tuning is performed using the improved sparrow search algorithm (ISSA), optimizing model parameters for improved accuracy and robustness. It uses the QIN-Breast Dataset to assess the suggested framework, demonstrating its effectiveness in accurately detecting Breast Cancer (BC) in PET images. Overall, this study presents a comprehensive and integrated approach for breast cancer detection, in clinical practice, may improve early diagnosis and treatment.

Keywords: Breast Cancer, Computer-Aided Detection, Averaging Filter, feature selection, improved sparrow search algorithm (ISSA), Classification.

1. Introduction

Breast cancer rates as the second most common cause of mortality for women worldwide and is one of the most common diseases [1]. Unchecked growth of cells and reproduction within breast tissue is its defining feature. Unlike normal cells, these cancerous cells divide and expand at an abnormally fast rate, leading to the development of a tumor or cell cluster. Furthermore, there is a chance that they could spread to other bodily parts, using a process known as metastasis, which includes the lymph nodes. Breast cancer typically originates from cells within other breast tissues, such as the milk-producing ducts or glandular lobules. As it has the highest rates of morbidity and death among diseases affecting women,

this disease presents severe risks to women's health and life [2]. Given its substantial risk, it is a concern that demands attention from everyone [3]. Breast cancer affects one in every eight women worldwide, making it a significant health concern. In 2022, In the United States, the American Cancer Society projects that there will be 609,360 cancer-related deaths and 1,918,030 new cases of the disease. 19% of those instances and 30% of all malignancies diagnosed in women are breast cancers [4]. In addition, the World Health Organization (WHO) predicts that around 19.3 million new cases of cancer would be discovered worldwide by 2025 [5].

The lack of defined protocols, the need for highly qualified pathologists, and the inherent subjectivity of the procedure make manual diagnosis of this life-threatening disease a difficult and demanding task. Diagnoses can vary between pathologists, even when evaluating the same patient [6]. Breast Cancer Care reports that 42% of National Health Service (NHS) trusts indicated a shortage of adequately trained staff to provide specialized breast cancer nursing support [7]. An automated method is necessary to assist radiologists identify and categorize breast cancer. One key solution involves the analysis of medical images, which can be obtained through various techniques such as Ultrasound, MRI, Mammography, X-ray, Sonography, SPECT, PET, and optical imaging [8]. In recent years, researchers have developed numerous machine learning (ML) and deep learning (DL)methods to aid in breast cancer diagnosis and classification. While these techniques have delivered promising results, they still face limitations when applied to Medical Image (MI) Analysis (MIA).

The way neurons in the human brain process information served as the inspiration for the ML area referred to as DL. Its core building blocks are small units known as artificial neurons, which are organized in multiple layers. These neurons are interconnected through weighted links that connect each one to others in the layer beneath it. To address complex issues or advance existing research, academics from a variety of disciplines are recently inspired to approach DL due to its increasing popularity [9].

For the purpose of determining the effectiveness of the suggested method in BCD and BC diagnosis, assessing the comparison of DL's performance in PET imaging with other methods are crucial. Here, the factors like interpretability, computational efficiency, and generalization ability were considered for this analysis. For the better growth and assessing optimal DL models in this field, interdisciplinary collaborations among experts in MI, ML, and oncology are crucial.

This work's primary impact lies in proposing a comprehensive framework for processing and analyzing PET images in the context of BC detection. Here's a breakdown of the contributions:

The following briefly summarizes the main contributions of this study:

1. Integrated Framework for Breast Cancer Detection.
   - A comprehensive pipeline is developed, encompassing noise removal, segmentation, feature extraction, feature selection, classification, and hyperparameter tuning—offering a unified approach for more reliable breast cancer detection in PET images.
2. Novel Denoising and Segmentation Techniques
   - A Hyper-Averaging Filter (HAF) is introduced for effective noise suppression in PET images, enhancing image clarity and diagnostic accuracy.
   - An Improved BIRCH algorithm is employed for precise segmentation, enabling the clear delineation of regions of interest (ROIs) for subsequent analysis.
3. Advanced Feature Extraction and Selection
   - Gray-Level Zone Length Matrix (GLZLM) features are extracted to capture detailed textural characteristics of breast tissue, providing deeper insight into potential cancerous regions.
   - mRMR method efficiently identifies the most salient features, reducing data dimensionality and enhancing classification performance.
4. Proposed O-IBGC-BiLSTM Classification Model

A hybrid optimized Inspection Boosted Graph Convolutional Bidirectional LSTM (O-IBGC-BiLSTM) model is introduced, combining:

   - Graph Convolutional Networks (GCNs) for spatial FE and relationship modeling among image patches.
   - Bidirectional LSTM units for capturing temporal dependencies in the data, increasing the classification accuracy of breast cancer.
5. Improved Sparrow Search Algorithm (ISSA) for Hyperparameter Tuning
   - Hyperparameters of the proposed classification model are fine-tuned (FT) using ISSA, which enhances the model’s accuracy and robustness, ensuring optimal performance under various clinical conditions.

6. Comprehensive Evaluation on QIN-Breast Dataset
   - The proposed framework is rigorously validated on the QIN-Breast Dataset, demonstrating its effectiveness and potential for assisting in early breast cancer diagnosis and improving treatment outcomes in a clinical setting.

2. Related Works

Sushanki et al [10] the research included most recent developments overview in multimodal imaging methods for the identification of breast cancer. Breast lesions may be more thoroughly observed by combining machine learning and deep learning techniques with radiomics, a quantitative study of imaging data. These methods assist in identifying benign and malignant tumors, offering valuable insights to physicians. Novel methods have been developed to improve steps like classification, segmentation, and feature extraction using a number of imaging modalities at different stages of BC diagnosis.

Abdullakutty et al [11] in particular, the research examined the integration of histopathological imaging (HI) with non-image data, which is an emerging field of multi-modal techniques. The study intends to improve diagnostic precision, encourage patient participation, and increase clinician confidence by using multi-modal data and placing an extreme value on explainability. This will eventually lead to more individualized approaches to treating breast cancer.

Oyelade et al [12] presented a new deep learning technique which incorporating the TwinCNN techniques to overcome challenges in breast cancer image identification across multiple modalities. The initial phase was to extract high-level (HL) and low-level (LL)features using networks incorporated with TwinCNN to perform modality-specific feature learning. Furthermore, to address the well-known problem of high-dimensional (HD) feature spaces, an enhanced binary optimization technique was developed to efficiently eliminate non-discriminative features from the search space (SS).

Hu et al [13] novels approach for predicting breast cancer survival, known as GMBS, was introduced. To combine various patient data types and create reliable initial embeddings, this approach starts by describing a number of multi-modal fusion components. To efficiently record patient connections, GMBS then integrates a patient-patient graph development component. Finally, it utilizes of the intricate structural information included in the generated graph by using a GCN.

An original or composite dataset was used to create a U-Net-based model by Imokawa et al. [14]. An uptake shape classification head was included in this dataset. The Dice score was obtained by comparing the simulations using the Wilcoxon signed-rank test. This dice score determines the pixel-wise agreement among expected and actual reality. The classifications' accuracy was also evaluated. The potential for overfitting, particularly when working with sparse or unbalanced datasets, may be a drawback of a U-Net-based model for PET image BC.

The use of DL as an NR technique to enhance image quality by reconstructing using shorter time frames for data acquisition has increased, according to Tsukijima et al. [15]. A position-adaptive PET image NR technique's use of a deep denoising filter bank may have the disadvantage of being more computationally complex. Thus, it might restrict its application in clinical settings in real time.

The sensitivity of whole-body PET (WBPET) and dedicated breast PET (DbPET) in diagnosing invasive BC was investigated by Sueoka et al. [16] taking into account tumour size and biology. To evaluate the tumour biology based on clinic pathological features and the sensitivity of DbPET and WBPET in tumour diagnosis, a retrospective investigation was carried out.

3. Proposed Methodology

This integrated approach—combining advanced filtering, segmentation, feature extraction, feature selection, a powerful classification model, and optimized hyperparameter tuning—provides a robust framework for accurate and efficient breast cancer detection in PET imaging is provided in figure 1.

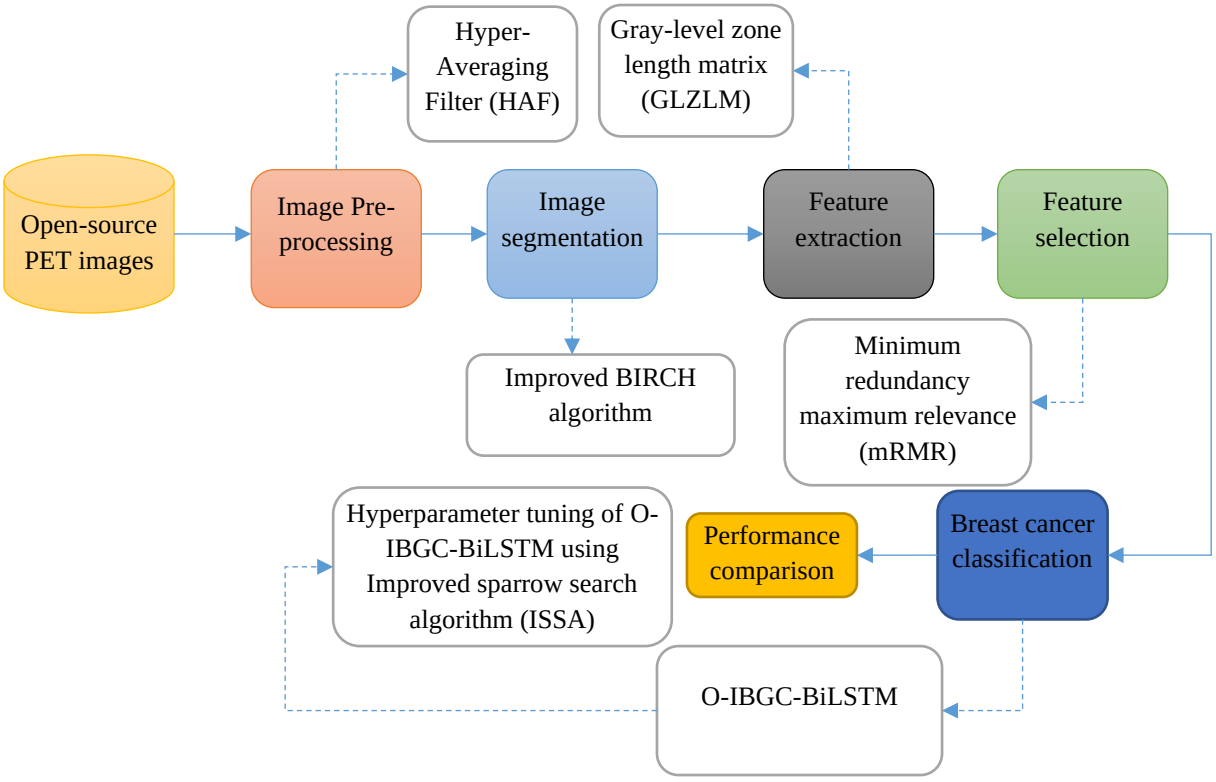

Figure 1: Structural design of suggested Framework

3.1 Dataset Description

The quantitative MR imaging (MRI) and longitudinal PET/CT scans in this dataset, and these are specifically collected to look into treatment assessment in BC in a pretreated condition. 3 vital phases were noted: prior to treatment initiation (t1), after the initial medication phase (t2), and either the second treatment round or the conclusion of all treatments before surgery (t3). A recently developed supporting apparatus enabled patients to assume and acquire PET/CT images in a prone position to make alignment with MRI data easier.

Distribution of benign and malignant cases: MI (such as MRI scans and mammograms) of breast tissues from both benign (non-cancerous) and malignant (cancerous) cases are included in the dataset. Different subsets or versions of the dataset may have different distributions of benign and malignant cases. Because BC is less common in MI datasets, there are typically a greater percentage of benign cases than malignant cases.

Demographics of subjects: Subject demographic data, such as age, gender, ethnicity, and pertinent medical history, may be included in the dataset. To comprehend how different factors may affect the diagnosis and detection of BC, demographic data is crucial.

214 investigations, 530 series, and 100,835 images totally with an aggregate image size of 11.286GB make up the dataset. The [QIN-Breast Dataset] (https://wiki.cancerimagingarchive.net/display/Public/QIN-Breast) is available to the public via the Cancer Imaging Archive (TCIA) website. This dataset is a valuable resource for the MI community, supporting improvements in early treatment evaluation techniques and improving BC management outcomes and patient care.

Researchers can efficiently train and assess machine learning models by the 80:20 section of the QIN-Breast dataset into training and testing sections. This ensures that the models are rigorously tested for their performance on hidden cases and trained on a sufficient amount of data.

3.2 Image Pre-processing Using HAF

Hyper-Averaging Filter (HAF) is introduced for effective noise suppression in PET images, enhancing image clarity and diagnostic accuracy. A variation of the conventional median filter (MF), the Dynamic Grade Weighted Switching MF (DGWSMF) dynamically modifies the filtering procedure according on local gradients, or "grades," of pixel intensity differences. It helps remove impulse noise (e.g., salt-and-pepper noise) and can adapt its filtering strength in uniform vs. edge regions. The limitation of DGWSMF is although the dynamic approach provides better edge handling than a standard median filter; it may still over smooth or slightly distort subtle PET-specific textural patterns. High-frequency

details important for accurate tumor delineation can be lost. So to overcome these issues, the HAF filter is used by offering superior edge preservation, multi-scale noise removal, and reduced parameter sensitivity.

HAF addresses these challenges by:

1. Multi-Scale Analysis: Integrating information across different levels of resolution to effectively remove both high-frequency and low-frequency noise.
2. Adaptive Weighting: Dynamically assigning weights based on local intensity variations, ensuring that edges and textures crucial for tumor detection remain intact.
3. Iterative/Selective Averaging: Using a local neighborhood approach where the filter adaptively averages pixel intensities, guided by statistical measures such as local variance or gradient [17].

A common strategy in HAF is to generate a multi-scale representation of the original noisy image I. Let:

$$I: \Omega \longrightarrow \mathbb{R}, \quad \Omega = \{(x,y) | 1 \le x \le M, 1 \le y \le N\} \qquad (1)$$

where $M \times N$ is the image size.

Create L scales $\{I_1, I_2, \dots, I_L\}$ from I, where each I_l can be obtained by:

- Applying Gaussian smoothing with different kernel sizes (or standard deviations).
- Using a wavelet/pyramid decomposition.
- Downsampling/upsampling mechanisms to explore image details at multiple resolutions.

Hence, I_1 might represent the finest scale (closest to the original resolution), and I_L might represent the coarsest scale.

At each scale l, define a local averaging operation over a window $W(x,y)$ centered at (x,y). The window size can be chosen based on typical tumor dimensions or noise characteristics in PET:

$$\hat{I}_l(x,y) = \frac{1}{|W(x,y)|} \sum_{(u,v) \in W(x,y)} I_l(u,v) \qquad (2)$$

Here, $\hat{I}_l(x,y)$ is the locally averaged intensity at scale l, and $|W(x,y)|$ represents the window's pixel number.

Compute a local variance or standard deviation $\sigma_l(x,y)$ at each scale l:

$$\sigma_l(x,y) = \sqrt{\frac{1}{|W(x,y)|} \sum_{(u,v) \in W(x,y)} (I_l(u,v) - \hat{I}_l(x,y))^2} \qquad (3)$$

Intuitively:

- A lower $\sigma_l(x,y)$ suggests a more homogeneous region, implying the local average $\hat{I}_l(x,y)$ could be more reliable.
- A higher $\sigma_l(x,y)$suggests greater local variation (edges, tumor boundaries), and we want to be cautious when averaging.

Based on $\sigma_l(x,y)$, derive a normalized weight $w_l(x,y)$. A common formulation is:

$$w_l(x,y) = \frac{\frac{1}{\sigma_l(x,y)+\epsilon}}{\sum_{k=1}^{L} \frac{1}{\sigma_k(x,y)+\epsilon}} \qquad (4)$$

To prevent division by zero, ϵ is a small constant. Scales with lower σ_l (more homogeneous) receive higher weight, while those with higher σ_l (likely edges/texture) are weighted less—yet still included to preserve crucial features. ϵ

The filtered intensity $\hat{I}_l(x,y)$ is determined as the sum of the weighted individual locally averaged intensities across all scales:

$$\hat{I}_l(x,y) = \sum_{l=1}^{L} w_l(x,y) \hat{I}_l(x,y) \qquad (5)$$

With $\sum_{l=1}^{L} w_l(x,y) = 1$

This aggregation ensures that each pixel intensity in the final image $\hat{I}$ is influenced primarily by the most reliable scales, striking a balance between noise reduction and detail preservation.

Algorithm 1: Hyper-Averaging Filter (HAF)

Input:
I (Noisy PET Image, size MxN)
L (Number of scales)
W (Window size or shape, e.g., 3x3, 5x5)
ε (Small regularization constant, e.g., 1e-6)
Output:
Î (Denoised PET Image)

Algorithm:
1. Construct Multi-Scale Representations:
   1.1. Initialize a set of images $S = \{\}$.
   1.2. For l = 1 to L:
   - Generate I_l from I by applying a smoothing or wavelet transform appropriate for scale l.
   - $S = S \cup \{I_l\}$.
2. Initialize I_{hat} as a zero matrix of size MxN.
3. For each scale l in $\{1, \ldots, L\}$:
   3.1. Compute local averages:
   For each pixel (x, y):
   - Define $W(x, y)$ as the neighborhood around (x, y).
   - Calculate local mean:

$$\hat{I}_l(x, y) = \frac{1}{|W(x,y)|} \sum_{(u,v) \in W(x,y)} I_l(u, v)$$

for all $(u, v) \in W(x, y)$.

   3.2. Determine the local standard deviation.
   For each pixel (x, y):

$$\sigma_l(x, y) = \sqrt{\frac{1}{|W(x,y)|} \sum_{(u,v) \in W(x,y)} (I_l(u, v) - \hat{I}_l(x, y))^2}$$

4. Compute Weights:
   For each pixel (x, y):

$$w_l(x, y) = \frac{\frac{1}{\sigma_l(x,y) + \epsilon}}{\sum_{k=1}^{L} \frac{1}{\sigma_k(x,y) + \epsilon}}$$

5. Aggregate Filtered Scales:
   For each pixel (x,y):

$$\hat{I}_l(x, y) = \sum_{l=1}^{L} w_l(x, y)\, \hat{I}_l(x, y)$$

6. Output the final denoised image $\hat{I}$.

3.3 Improved BIRCH algorithm for segmentation

An Improved BIRCH algorithm is employed for precise segmentation, enabling the clear delineation of regions of interest (ROIs) for subsequent analysis. Classical BIRCH uses a single, global threshold to decide whether a new data point (pixel) merges with an existing cluster or forms a new one [18]. However, this approach can be insufficient for medical images—particularly PET—where local intensity variations (e.g., tumor vs. healthy tissue) differ significantly. Hence, Improved BIRCH incorporates adaptive/local thresholds and additional refinements to handle the nuances of PET data more effectively. This adaptation addresses the variability and noise typical in PET data by incorporating local/adaptive thresholds and, optionally, weighted updates for cluster features.

Each cluster c in BIRCH is summarized by a Cluster Feature (CF):

$$CF(c) = \left(n, \sum_{i=1}^{n} x_i, \sum_{i=1}^{n} \|x_i\|^2 ,\right) \quad (6)$$

where:

- The number of pixels or voxels in the cluster is denoted by n,
- $\sum x_i$ is the data points' linear sum (useful for centroid calculation),
- $\sum \|x_i\|^2$ is the total of the data points' squared magnitudes (used to compute variance or radius).

From the CF, one can quickly derive:

1. Centroid of cluster c:

$$\mu_c = \frac{1}{n} \sum_{i=1}^{n} x_i \quad (7)$$

2. Radius / Variance (several definitions exist; one common approach is RMS radius):

$$RMS(c) = \sqrt{\frac{1}{n} \sum_{i=1}^{n} \|x_i - \mu_c\|^2} \quad (8)$$

A key improvement over classical BIRCH is to use local thresholds for merging decisions. For a cluster c define:

$$T_{local(C)} = \alpha \times RMS(c)$$

where α is a user-defined scaling factor. This allows clusters in areas of higher intensity variability (e.g., tumor regions) to have larger thresholds, thereby controlling when new points (pixels) merge or form separate clusters.

For PET images, certain pixels (e.g., very high or very low intensity) may reflect tumors or noise. To emphasize or de-emphasize specific intensities, one can introduce a weight w_{new} for each incoming data point x_{new}:

$$CF'(c) = \left(n + w_{new}, \sum_{i=1}^{n} x_i + w_{new} x_{new}, \sum_{i=1}^{n} \|x_i\|^2 + w_{new} \|x_{new}\|^2,\right) \quad (9)$$

w_{new} could be a function of intensity, e.g., placing higher weight on likely tumor intensities or lower weight on outliers/noise

Hence finally a CF Tree Structure is formed, Non-leaf nodes contain a list of CF entries representing summaries of their children. Leaf nodes store CF entries for actual "sub-clusters," each corresponding to a potential segment in the image.

3.4 Advanced Feature Extraction and FS using mRMR

Following segmentation, the GLCM, Grey-Level Run Length Matrix (GLRLM), and GLZLM in PET images of breast data are used to identify radiomic features beyond basic first-order intensity statistics [19]. The process typically follows a set of common steps, ensuring that extracted features are both consistent and clinically meaningful.

i. First-Order Features

Before extracting second-order or higher-order features, many pipelines begin by calculating first-order intensity-based features within the ROI, such as:

- Skewness, Kurtosis, Mean, Median, and Standard Deviation.
- Energy, Entropy, and Minimum and Maximum Intensity (from histogram).

These features only quantify pixel intensity distributions without considering spatial relationships.

ii. GLCM (Grey-Level Co-occurrence Matrix)

Construction

1. Pairwise Intensity Relationships: The GLCM tracks how often two pixels with specific intensities (i.e., grey levels $g_1$and g_2) occur next to each other (according to a given offset and direction).
2. The most common directional offsets are:

- 0^0(horizontal, right)
- 45^0(diagonal, top-right)
- 90^0(vertical, top)
- 135^0(diagonal, top-left)

For volumetric PET data, the GLCM can be extended to 3D directions, considering neighboring voxels in 26 possible orientations.

3. Matrix Size: If you discretize to N gray levels, the GLCM is an N × N matrix.

Common GLCM Indices

From each GLCM, you extract standardized texture indices, such as:

- Contrast: Emphasizes intensity differences between neighboring pixels.
- Homogeneity: Increases if neighboring intensities are similar.
- Energy (or Angular Second Moment): High if the co-occurrence matrix has dominant, repeated intensity pairs.
- Correlation: Measures the linear dependency of gray levels.

iii. GLRLM

Construction

1. Run Definition: A "run" is a set of consecutive pixels—along a specific direction—that share the same gray level.
2. Matrix Dimensions: Rows represent gray levels; columns represent run lengths (from 1 up to a maximum run length).
3. Directionality: Typically evaluated in horizontal, vertical, and possibly diagonal directions, then combined or averaged.

Common GLRLM Indices

- Short Run Emphasis (SRE): Highlights the prevalence of short, uniform runs.
- Long Run Emphasis (LRE): Weighs longer runs more heavily (indicating bigger uniform-intensity stretches).

- Gray-Level Non-Uniformity (GLNU): Assesses the distribution of runs across different gray levels.
- Run Length Non-Uniformity (RLNU): Checks how run lengths are distributed overall.

iv. GLZLM

Construction

1. Zone Definition: A "zone" is a contiguous region (in 2D or 3D) of pixels sharing the same intensity. Unlike runs (which are linear), zones can be any shape, connected in all directions.
2. Matrix Dimensions: Rows correspond to gray levels, columns to zone sizes (number of connected pixels).
3. Zone Identification: Use a region-growing or connected-component approach. For each identified zone (gray level g, size l), increment $GLZLM(g, l)$ by 1.

Common GLZLM Indices

- Small Zone Emphasis (SZE): Indicates the presence of multiple small contiguous zones.
- Large Zone Emphasis (LZE): Highlights large uniform regions.
- Gray-Level Non-Uniformity (GLNU): Focuses on how evenly or unevenly the gray levels form zones.
- Zone Length Non-Uniformity (ZLNU): Looks at the variability in zone sizes.

Hence combining all together and form a matrix below as

1. Compute Matrices: For each ROI in the breast PET image, construct:
   - One or more GLCMs (varying direction and/or offsets).
   - One or more GLRLMs (varying directions).
   - A single GLZLM (or separate 2D/3D-based matrices, depending on dimensionality).
2. Extract Features: From each matrix, calculate the standardized feature indices (like Contrast, SZE, GLNU, etc.). The result is a feature vector describing local texture properties in the segmented breast region.

The features are then applying a selection method using mRMR to reduce dimensionality and pick the most predictive ones. The mRMR method efficiently identifies the most salient features, reducing data dimensionality and enhancing classification performance [20].

The mRMR approach is to select a subset of characteristics that:

1. Maximize the Relevance to the intended audience (e.g., benign vs. malignant).
2. Minimize Redundancy among themselves, so selected features contribute complementary information rather than duplicating each other.

mRMR relies on Mutual Information (MI) to quantify both relevance and redundancy. The MI between two variables X and Y is defined as:

$$I(X;Y) = \sum_{x\in\chi}\sum_{y\in y} p(x,y)\log\left(\frac{p(x,y)}{p(x)p(y)}\right) \quad (10)$$

where:

- $p(x,y)$ is the function of X and Y's combined probability distribution.
- $p(x)$ and $p(y)$ are X and Y's respective marginal distributions.

A larger MI means a stronger statistical dependence/relationship.

Next the Relevance and Redundancy is calculated as

- Relevance of a feature f with respect to the target class C: measured by $I(f; C)$.
- Redundancy between two features f_i and f_j: measured by $I(f_i; f_j)$.

Finally mRMR Criterion is

Let F be the full feature set (e.g., all GLCM, GLRLM, GLZLM features) and S be the subset of features chosen so far. The mRMR algorithm chooses the next feature $f \in F \setminus S$ by maximizing:

$$\text{mRMR Score}(f) = I(f;C) - \frac{1}{|S|}\sum_{f_s\in S} I(f;f_s) \quad (11)$$

Algorithm 2: Applying mRMR to GLCM, GLRLM, and GLZLM Features

```
Inputs:
  F = {f_1, f_2, ..., f_N}   # Complete set of GLCM, GLRLM, GLZLM features
  C = class labels           # e.g., benign or malignant
  M = desired number of features to select
  # Precompute Mutual Information (MI) tables:
  # Rel(f) = I(f; C) for each f in F
  # Red(f_i, f_j) = I(f_i; f_j) for each pair (f_i, f_j)
```

Output:
S (selected feature subset)

Algorithm:
1. Initialize:
$S = \emptyset$ # empty set of selected features
2. # Step 1: Select the most relevant feature
$f_{best} = \underset{f \in F}{\text{argmax}}\ \text{Rel}(f)$
Add f_{best} to the selected subset:
$S = S \cup \{ f_{best} \}$
Remove f_{best} from F.
3. # Step 2: Iteratively select next features
while $|S| < M$:
$\text{maxScore} = -\infty$
chosenFeature = None
for each f in F:
# Compute the difference-based mRMR score
$\text{Score}(f) = I(f; C) - \frac{1}{|S|}\sum_{f_s \in S} I(f; f_s)$
if $\text{score} > \text{maxScore}$:
$\text{maxScore} = \text{score}$
chosenFeature = f
# Add the chosen feature to S
$S = S \cup \{ \text{chosenFeature} \}$
$F = F \setminus \{ \text{chosenFeature} \}$
return S

Hence Using mRMR with GLCM, GLRLM, and GLZLM features from breast PET data provides a systematic way to select the most informative textural descriptors while avoiding redundancy. The approach relies on mutual information to balance each feature's relationship to the class (relevance) against its overlap with already-selected features (redundancy). The result is a concise, powerful subset of radiomic features optimized for downstream tasks like tumor classification.

3.5 Proposed O-IBGC-BiLSTM -ISSA Classification Model

The O-IBGC-BiLSTM model is an innovative deep learning architecture designed for breast cancer classification in PET images. It combines Graph Convolutional Networks (GCNs) which capture complex spatial relationships among image features with BiLSTM units, may model temporal connections by processing data both forward and backward.

A key component of this model is the Scrutiny Boosting mechanism, which refines the learning process by focusing on the most informative features, thereby improving classification accuracy.

3.5.1 Graph Convolutional Neural Network

A versatile and successful technique for learning graph-structured data representations is GCNN. Across a range of tasks, many GCNN modifications have produced state-of-the-art outcomes [21] [22]. Using skeleton edge sets, let $\mathbb{G}_t = \mathbb{V}_t$, where $\mathbb{V}_t$ represents N joint nodes and E_t represents a graph G of input data at time t for action recognition. Definition of $\mathbb{V}_{ti}$ neighbours.

$$N(\mathbb{V}_{ti}) = \mathbb{V}_{ti} | d(\mathbb{V}_{ti}, \mathbb{V}_{tj}) \leq D \qquad (12)$$

Eq (12) converts $\mathbb{V}_{tj}$ to $\mathbb{v}_{ti}$. $\mathbb{V}_t$ 1,2 ……, K represents the assigned labels in the graph labelling function lab. Nodes $\mathbb{V}_{tj} \in \mathbb{V}_{ti}$ are partitioned into K subsets from the surrounding set $N(\mathbb{V}_{ti})$. Computers can use graph convolutions.

$$Y_{output}(\mathbb{V}_{ti}) = \sum_{\mathbb{v}_{ti} \in N(\mathbb{V}_{ti})} \left(\frac{1}{Z_{ti}(V_{ti})}\right) X(V_{ti}) \mathbb{W}(\text{lab}(\mathbb{V}_{ti}) \qquad (13)$$

The nodes' ($\mathbb{V}_{tj}$) characteristics are represented by $X(\mathbb{V}_{tj})$ in Eq (13). Weights are assigned and indexed by labels $\text{lab}(\mathbb{V}_{tj})$ from K weights using the weight function implied by W(.). The equivalent subset that normalizes characteristics is denoted by $Z_{ti}(\mathbb{V}_{tj})$. The graph convolutions' outputs at node $\mathbb{V}_{tj}$ are represented as $Y_{output}(\mathbb{V}_{ti})$. In particular, eq. (14) may be expressed using neighbouring matrices as

$$Y_{output} = \sum_{(k=1)}^{k} V_k^{(-1/2)} AMK V_k^{(-1/2)} X\mathbb{W}_k \quad (14)$$

where in eq (14), $(AM)_k$ existing in the label's spatial arrangement as the adjacency matrix $k \in 1, 2, \ldots . K$. $\wedge_k^{ii} = \sum_j AM_k^{ij}$ is a degree matrix.

3.5.2 Inspection boosted Graph Convolutional BiLSTM

Long-term temporal dependencies for sequence modelling are especially well-managed by LSTM, a form of recurrent neural network (RNN), as multiple studies have shown. To analyze the temporal dynamics of skeletal sequences, a number of LSTM-based models have been used. However, in skeleton-based action detection, the fully connected operator in LSTM restricts its ability to disregard spatial correlations [23] [24]. IBDC-LSTM surpasses LSTM in identifying unique characteristics in spatial configurations and temporal dynamics, and assessing the relationship between co-occurrence in spatial and temporal domains. As LSTM, IBGC-LSTM contains three gates: i_t, forget f_t, and o_t. However, graph convolution operators create these gates. Cell memory, IBGC-LSTM input X_t, and hidden state H_t. Data in C_t is graphed. Graph convolution enables IBGC-LSTM's hidden state H_t and cell memory C_t moves spatially and dynamically. Graph convolution computations are performed through the internal operator of IBGC-LSTM, as contrast to LSTM. Using this method, significant nodes' attributes are improved so they may present additional distinctive information. The IBGC-LSTM units perform the following functions:

$$i_t = \sigma(\mathbb{W}_{xi}.\mathbb{G}X_t + \mathbb{W}_{hig}.\mathbb{G} \times H_{t-1} + b_i) \quad (15)$$

$$f_t = \sigma(\mathbb{W}_{xf}.\mathbb{G}X_t + \mathbb{W}_{hfg}.\mathbb{G} \times H_{t-1} + b_t) \quad (16)$$

$$o_t = \sigma(\mathbb{W}_{xo}.\mathbb{G}X_t + \mathbb{W}_{hog}.\mathbb{G} \times H_{t-1} + b_o) \quad (17)$$

$$cm_t = f_t \odot cm_{t-1} + i_t \odot mi_t \quad (18)$$

$$cm_t = f_t \odot cm_{t-1} + i_t \odot mi_t \widehat{H}_t = og_t \odot \tanh(Cm_t) \quad (19)$$

$$\widehat{H}_t = o_t \odot \tanh(Cm_t) \quad (20)$$

$$H_t = f_{att}(\widehat{H})_t + (\widehat{H})_t \quad (21)$$

Eq (4)-10, where.G denotes graph convolution operators and ⊙ indicates Hadamard products. A sigmoid activation function is represented as σ(.). The modulated inputs are represented by mi_t. Intermediate hidden states are H_t. The sum of $f_{att}(\widehat{H})_t$ and $(\widehat{H})_{tas}$ the method improves information at crucial nodes while diminishing the data at less relevant nodes, with the objective of maintaining the accuracy of spatial data. To enable the scrutiny network to adaptively concentrate on important joints, a soft scrutiny mechanism is used to automatically assess the relevance of joints. An example of a spatial inspection network is provided by equations (15) through (21). Important temporal dynamics and spatial structure information $(\widehat{H})_t$ of the IBGC-LSTM are present in the intermediate hidden state.

In the Bidirectional LSTM (BiLSTM), two LSTMs are used: The sequence is processed from start to end by one LSTM and from end to beginning by the other. Finally, both LSTMs' outputs are merged, usually through concatenation.

The forward and backward LSTM outputs will be represented as $h_t^{(f)}$ and $h_t^{(b)}$, respectively. At every time step, the final output is:

$$h(t) = \left[h_t^{(f)}, h_t^{(b)}\right] \quad (22)$$

To further enhance performance, the Improved Sparrow Search Algorithm (ISSA) is employed for hyperparameter tuning, ensuring that the model's parameters are optimally configured for robust and accurate breast cancer detection.

3.5.3 An Improved Sparrow Search Algorithm for Optimizing O-IBGC-BiLSTM

The SSA consists of two primary roles: producers and scroungers. Additionally, certain sparrows are responsible for reconnaissance and early warning. It is essential to improve both producers' and scroungers' positions in SSA, as well as the mechanisms related to reconnaissance and early warning. Producers, characterized by high fitness levels, have a wide search range and lead the sparrow population in exploration. Scroungers, in pursuit of better fitness, to get more energy, either go to various locations or follow the producers to forage. Meanwhile, some newcomers monitor discoverers and seize their resources. When sparrows sense the threat of predators, they swiftly activate anti-predation strategies [25] [26].

The Sparrow Search Algorithm (SSA) simulates sparrow foraging for the best solution in the solution space. The sparrow population X consists of n individuals, each characterized by m dimensions, which may be expressed as follows:

$$X = \begin{bmatrix} x_{1,1} & x_{1,2} & \cdots & x_{1,m} \\ x_{2,1} & x_{2,2} & \cdots & x_{2,m} \\ \vdots & \vdots & \ddots & \vdots \\ x_{n,1} & x_{n,2} & \cdots & x_{n,m} \end{bmatrix} \quad (23)$$

The following is the expression for each sparrow's fitness value F_X:

$$F_X = \begin{bmatrix} f([x_{1,1} & x_{1,2} & \cdots & x_{1,m}]) \\ f([x_{2,1} & x_{2,2} & \cdots & x_{2,m}]) \\ \vdots & \vdots & \ddots & \vdots \\ f([x_{n,1} & x_{n,2} & \cdots & x_{n,m}]) \end{bmatrix} \quad (24)$$

where $f(\cdot)$ represents the fitness function value.

In formula (3), the producer's update position is shown. In general, 10% to 20% of the sparrow population is made up of the producer:

$$X_{i,j}^{t+1} = \begin{cases} X_{i,j}^{t} \cdot \exp\left(-\frac{1}{\alpha \cdot iter_{max}}\right) & \text{if } R_2 < S_T \\ X_{i,j}^{t} + Q \cdot L & \text{if } R_2 \geq S_T \end{cases} \quad (25)$$

$X_{i,j}^{t}$ are the number of iterations and the ith sparrow's present location in the jth dimension. A random integer α (0,1), a maximum number of iterations $iter_{max}$, a normal distribution random number Q, and a 1*m matrix L with all elements equal to 1 are used. The warning and safety values are $R_2 \geq S_T$. $R_2 \in$ [0,1] and $S_T \in$ [0.5,1]. When $R_2 \geq S_T$, the population's foraging environment is safe, predators are not present, and extended search is possible. The sparrow population must relocate to avoid predators, as shown by

The position update for scroungers is determined by formula (26). In the sparrow population, all individuals, except for the producer, function as scroungers.

$$X_{i,j}^{t+1} = \begin{cases} Q \cdot \exp\left(-\frac{X_{worst} - X_{i,j}^{t}}{i^2}\right) & \text{if } i > \frac{n}{2} \\ X_{p}^{t+1} + \left|X_{i,j}^{t} - X_{p}^{t+1}\right| \cdot A^{+} \cdot L \cdot & \text{if } i \leq \frac{n}{2} \end{cases} \quad (26)$$

where the current global optimum position is denoted by X_{best}^{t}. f_i is the sparrow individual's fitness value (FV), the current best and worst FV in the world are represented by f_w and f_g, β is the control parameter for step size that adheres to the (0,1) normal distribution, ε is the smallest constant that prevents the denominator from going to zero, and K is a random integer between [-1,1]. When $f_i = f_g$, The center sparrow should proceed near to other sparrows to lessen the possibility of predation since it is aware of the threat; when $f_i > f_g$, the sparrow must relocate to the worldwide ideal place as it is on the periphery of the population and is difficult to caught.

3.5.3.1 Improved SSA

The SSA algorithm's starting population distributes unevenly over the search space, which results in a slow pace of convergence, low ergodicity, and limited population selection. In addition, the search procedure is insufficient at the start of the iteration due to the rapid get and smaller disturbance range caused by the e^{-x} exponential function in equation (3). However, in the middle and later stages, the decline slows down while the disturbance range becomes excessively large, which hampers convergence and increases the likelihood of getting trapped in local optima. By optimizing the starting population and the search strategy, this study improves the SSA method to handle these issues.

1) Optimal initial population using Improved sine chaos map

Researchers often use chaotic mapping to solve the problem of unequal beginning population distribution because of its unpredictability, ergodicity, and intrinsic regularity. Modifying the sine trigonometric function produces the sine map; however, it lacks uniform distribution in the phase plane, resulting in significant variations in distribution probability. In a study, an improved sine chaotic map was shown, and the system model was expressed as follows:

$$\begin{cases} a_{i+1} = \sin(\mu \pi a_i) \\ b_{i+1} = \sin(\mu \pi b_i) \\ y_{i+1} = (a_{i+1} + b_{i+1}) \bmod 1 \end{cases} \quad (27)$$

The control parameter μ may be any real integer, but the starting values, a_0 and b_0, are both random numbers in the interval [0,1]. An equal distribution of the chaotic system throughout the phase plane occurs when μ is a real number with an absolute value greater than 1000. Mod stands for modulo operation, while y_{i+1} is the value of the chaotic sequence produced by iteration.

2) Introduction dynamic adaptive weight to improve the optimization strategy

The dynamic weight ω of the algorithm is crucial for maintaining balance between local and global search. By allowing the system to modify its approach to searching, a broader exploration range can be achieved. To enhance the sparrow population's large-scale search capability, a larger weight must be assigned.

In this study, to improve the search efficiency, the producer position update formula (24) is modified to include dynamic adaptive weights. Formula (28), which gives the mathematical equation for ω.

$$\begin{cases} a(t) = \exp\left(2 \cdot \frac{1-\sin(\pi t)}{iter_{max}}\right) - \exp\left(-2 \cdot \frac{1-\sin(\pi t)}{iter_{max}}\right) + \alpha \\ b(t) = \exp\left(2 \cdot \frac{1-\cos(\pi t)}{iter_{max}}\right) + \exp\left(-2 \cdot \frac{1-\cos(\pi t)}{iter_{max}}\right) + \beta \\ \omega(t) = \frac{a(t)}{b(t)} \end{cases} \quad (28)$$

where $iter_{max}$ is the algorithm's maximum iteration count, and both α and β are random values in [0,1]. Figure 2 shows the ω function image.

Formula (29) shows the update formula for the producer position with the addition of ω.

$$X_{i,j}^{t+1} = \begin{cases} \left(X_{i,j}^{t} + \omega \cdot \left(f_{ib}^{t} = X_{i,j}^{t}\right)\right) \cdot \alpha, & \text{if } R_2 < S_T \\ \omega \cdot X_{i,j}^{t} + Q \cdot L & \text{if } R_2 \geq S_T \end{cases} \quad (29)$$

In formula (8), α is a random integer in [0, 1], and f_{ib}^{t} is the optimum fitness in the current iteration.

3) Improved SSA steps

The procedure for the ISSA, the following describes this approach, which incorporates adaptive dynamic weights and enhanced sine chaos mapping:

Step1. Indicate parameters. The population size n, producers P_D, reconnaissance and early warning sparrows S_D, early warning value R_2, and solving problem dimension m are provided. Consider the upper and lower limits (ub, lb) and the maximum iteration number $iter_{max}$.

Step 2. Develop a sparrow population X: n × m then map it into the original problem's solution space using formula (27)'s augmented sine chaotic map sequence.

Step 3. Select the optimum fitness value f_g and the worst fitness value f_w for the sparrow, and record the position information X_{best} and X_{worst}.

Step 4. Select the producers. All other sparrows are scavengers, and only those with higher fitness values are chosen as producers based on the predetermined ratio P_D. The modified formulas (29) and (25), respectively, are used to update the positions of producers and scroungers.

Step 5. Using the formula (26), update the positions of S_D reconnaissance and early warning sparrows gathered at random.

Step 6. If the method has reached the maximum iterations, the loop returns the optimization result $iter_{max}$ or the accuracy of the solution; if not, return to step 3.

Algorithm 3: O-IBGC-BiLSTM-ISSA for Classification

```
# Step 1: Initialize the O-IBGC-BiLSTM model
O_IBGC_BiLSTM = initialize_O_IBGC_BiLSTM()
# Step 2: Apply ISSA for hyperparameter tuning
Initialize sparrow population using Improved Sine Chaos Map
for iteration in range(max_iterations):
    for each sparrow in population:
        # Evaluate fitness of the O-IBGC-BiLSTM with current sparrow parameters
        fitness = evaluate_fitness(O_IBGC_BiLSTM, sparrow)
            # Update the producer and scrounger positions
    update_producer_position()
    update_scrounger_position()
    # Apply Graph Convolution and Scrutiny Mechanism
    O_IBGC_BiLSTM = apply_GCN_and_Inspection(O_IBGC_BiLSTM)
        # Train O_IBGC_BiLSTM with updated features
    O_IBGC_BiLSTM = train(O_IBGC_BiLSTM)
        # Re-evaluate fitness and update positions
    evaluate_fitness(O_IBGC_BiLSTM)
    update_sparrow_positions_based_on_fitness()
```

```
    # If termination condition is met, exit
    if convergence_reached():
        break
# Step 3: Final retraining with optimal parameters
train_final_model(O_IBGC_BiLSTM)
return final_classification
```

4. Experimental Results and Discussion

An 80-20 split is used for training and testing in order to set up an experimental pipeline in MATLAB for training a DL model on the QINbreast PET imaging dataset.
The Table 1 provides the implementation details.

Table 1: Implementation Requirements

Component	Details
Software	MATLAB 2023b
Required Toolboxes	Deep Learning Toolbox, Image Processing Toolbox, Statistics and ML Toolbox, Graph and Network Algorithms Toolbox, Parallel Computing Toolbox
Operating System	Windows 10
GPU	NVIDIA RTX 3080 or higher (for deep learning acceleration)
CPU	Intel Core i9
RAM	Minimum 16 GB (Recommended 32 GB)
Storage	Minimum 500 GB SSD

The QIN-BREAST dataset, available through The Cancer Imaging Archive (TCIA), is a comprehensive collection of imaging data aimed at facilitating research in breast cancer treatment assessment, particularly in the neoadjuvant setting. Pre-processing involves image resizing, normalisation, and augmentation after data loading. Both subsets are randomly selected from the dataset using the suggested O-IBGC-BiLSTM-ISSA architecture. It ensures that the distribution of cancerous and non-cancerous samples is balanced. With training parameters like batch size and learning rate set, this recommended approach is selected and put into practice. The model is then trained using the training subset, with measures like accuracy (Acc) and loss being used to track training progress. Test the trained model's recall (R), accuracy (P), and accuracy (Acc) in the testing subset after that. In order to gain insights for possible improvements, visualisations help interpret the model's predictions and comprehend its behaviour.
The localisation of masses and the classification of observed masses are thus the two main stages of the suggested framework. The input sample image and the corresponding segmentation image are shown in Fig. 2. The effectiveness of the mass categorisation is evaluated using some performance measures, while the accuracy of lesions detection is evaluated using others. Here, the Intersection Over Union (IOU) metric in breast mammography indicates the algorithm's level of accuracy in localising cancers in the following manner:

$$\mathrm{IOU} = \frac{\mathrm{AO}}{\mathrm{AU}} \tag{30}$$

Where AO is Area of Overlap and AU is Area of Union. An accurate detection of the mass in this study is defined as an IOU larger than or equal to 0.5; otherwise, the detection is unnoticed. Following a particular classifier that detects the tumor category of each localized mass, one of four results may be obtained by comparing it to the initial data that was provided. The first is a benign tumor that is misclassified as tumors (False Positive (FP)), while the second is a benign growth that is really malignant (True Positive (TP)). The same is true when a benign tumor is erroneously classified as malignant (False Negative (FN)) and then again as malignant (TP). The confusion matrix, one of the essential metrics used to assess classification accuracy, mostly comprises these four metrics. The comparison techniques are Oriented Faster Region based Convolutional Neural Network (OFRCNN) [23], DL aided Efficient Adaboost Algorithm (DLA-EABA) [28], You Only Look Once (YOLO)-V4 [27], and NeuroPET. Equations (31) to (34) were used to compute the following using the measured TN, FN, FP, and TP.

$$\text{Precision} = \frac{\mathrm{TP}}{\mathrm{TP} + \mathrm{FP}} \tag{31}$$

$$\text{Recall} = \frac{\mathrm{TP}}{\mathrm{TP} + \mathrm{FN}} \tag{32}$$

$$\text{Overall accuracy} = \frac{\text{TP} + \text{TN}}{\text{TP} + \text{FN} + \text{TN} + \text{FP}} \quad (33)$$

$$\text{F1} - \text{score} = 2 * (\text{Precision} * \text{Recall}) / (\text{Precision} + \text{Recall}) \quad (34)$$

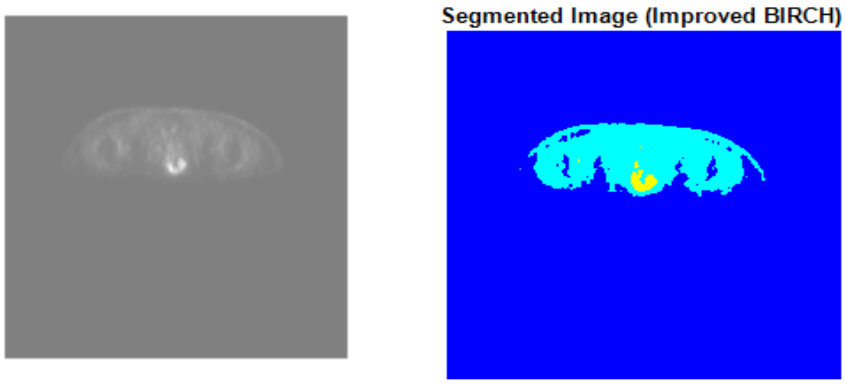

Figure 2: Input image and segmentation image

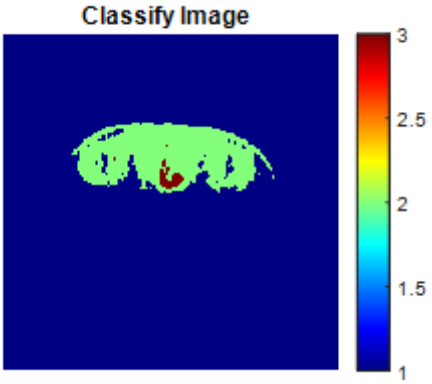

Figure 3: Classified Image

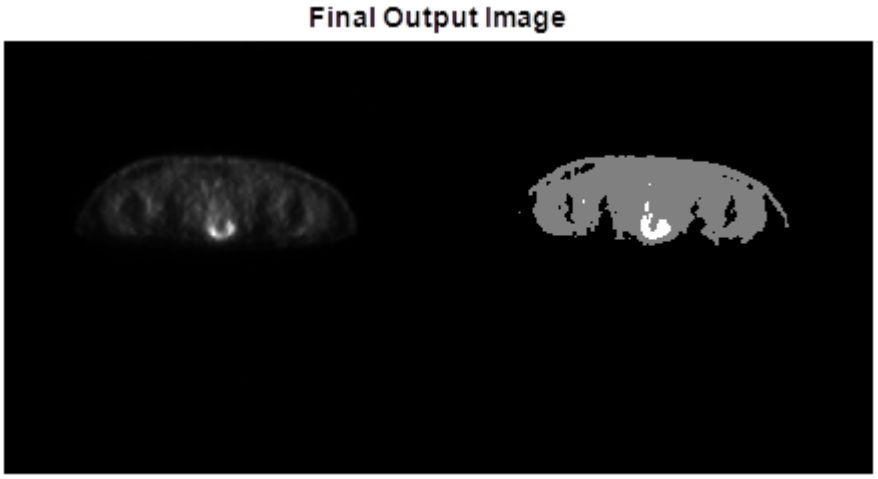

Figure 4: Final Output Image

Table 2 compares the performance of five different models—DLA-EABA, YOLO-V4, OFRCNN, NeuroPET, and the suggested O-IBGC-BiLSTM-ISSA across multiple performance metrics commonly used in classification tasks: Acc, P, R, F-Measure, and Error. Each metric provides insights into different aspects of model performance, and understanding these helps assess how well each model performs in breast cancer classification from PET images (or similar tasks).

Table 2: The statistical result of recommended and existing methods based on several performance metrics

Metrics	DLA-EABA	YOLO-V4	OFRCNN	NeuroPET	O-IBGC-BiLSTM-ISSA
Acc	80	91	92.60	95.02	96.51
P	76.12	80	81.38	91.48	95.41
R	82.12	83.40	93.62	95.06	96.64
F-Measure	78.10	81.66	87.07	93.24	96.02
Error	20	9	7.3	4.9	3.4

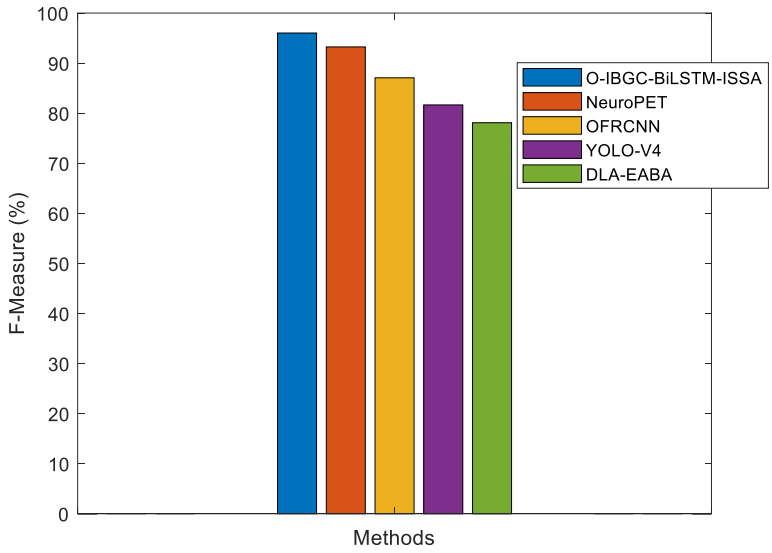

Figure 5: F-measure Comparison of the suggested and current approaches

The analysis of comaprison in Fig.5 illustrates the precision of recommended classifiers including YOLO-V4, DLA-EABA, OFRCNN, NeuroPET and O-IBGC-BiLSTM-ISSA. As depicted in the graph, the proposed O-IBGC-BiLSTM-ISSA technique shows a remarkably greater F-measure value in comparison to the other methods, reaching an impressive 96.02%. Conversely, the f-measure value of current approaches is commendable but slightly lower, with YOLO-V4, DLA-EABA, OFRCNN and NeuroPET achieving precision values of 81.6646%, 78.1%, 87.0749 % and 93.24% respectively. The combination of DL methods with optimization algorithms in the proposed O-IBGC-BiLSTM framework demonstrates a holistic approach towards achieving higher accuracy in BC classification from PET images.

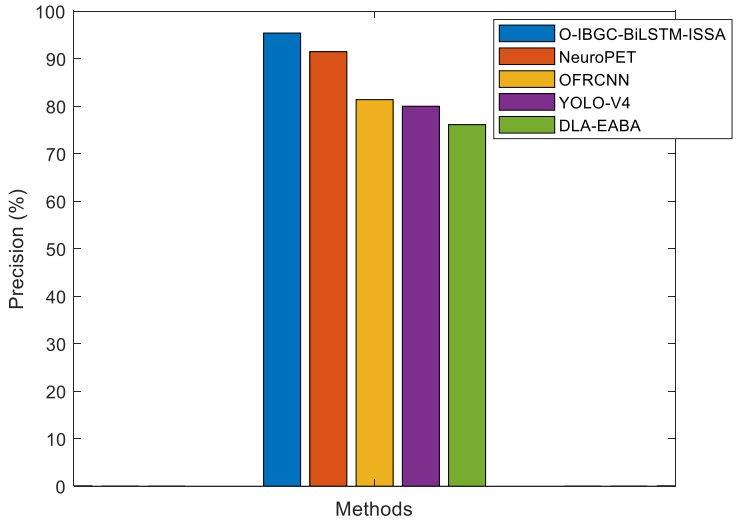

Figure 6: Precision Comparison of the proposed and existing approaches

The comparison outcomes of the P among the suggested YOLO-V4, DLA-EABA, OFRCNN, NeuroPET and O-IBGC-BiLSTM-ISSA classifiers are presented in Fig.6. According to the graph, the proposed O-IBGC-BiLSTM-ISSA method exhibits a remarkable P rate compared to the current methods. With a precision rate of 95.41 %, O-IBGC-BiLSTM-ISSA proves to be an efficient approach for detecting attacks with exceptional accuracy.

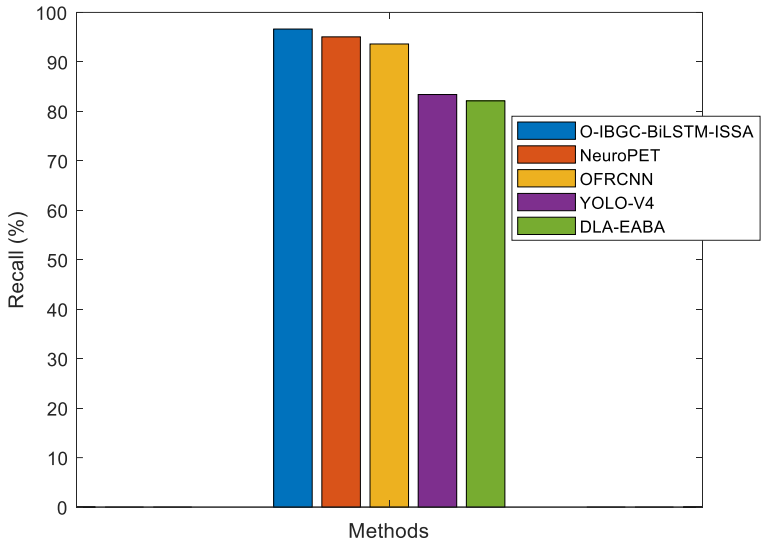

Figure 7: Recall Comparison of the proposed and existing approaches

The comparison outcomes of the R for the suggested YOLO-V4, DLA-EABA, OFRCNN, NeuroPET and O-IBGC-BiLSTM-ISSA are depicted in Figure 7. Notably, the proposed O-IBGC-BiLSTM-ISSA approach exhibits an exceptionally high recall rate of 96.64%, indicating its ability to effectively identify relevant instances. Specifically, the suggested OFRCNN also demonstrates a high recall rate, underscoring its capability in accurate detection recognition. In comparison, existing approaches such as YOLO-V4, DLA-EABA, OFRCNN and NeuroPET offer recall rates of 83.4%, 82.12%, 93.6212% and 95.06% respectively. These findings suggest that the proposed scheme outperforms previous techniques in disease recognition outcomes. Utilizing spiking neural network dynamics allows the model to capture temporal dependencies in the input data. The strong segmentation, direct training for BC classification, efficient weight selection utilising ISSA of the O-IBGC-BiLSTM-ISSA framework, and complete feature learning capabilities are all responsible for the high R it achieved.

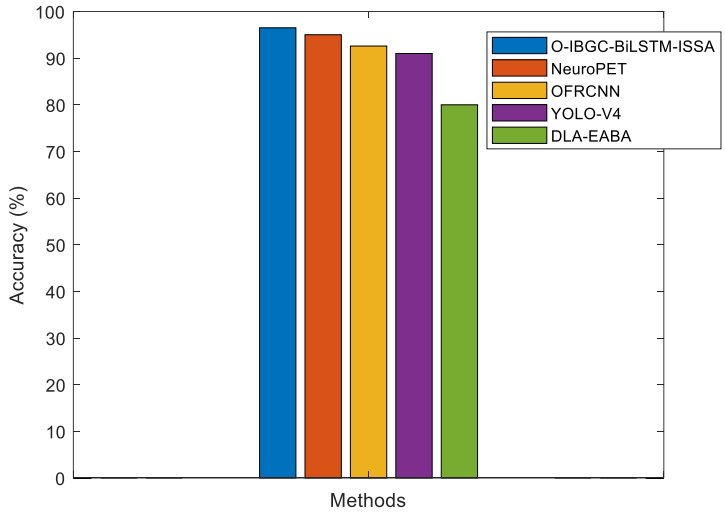

Figure 8: Accuracy Comparison of the suggested and current methods

The graph presented in Fig.8provides an overview of the Acc comparison for (AD) attack detection utilizing methods including YOLO-V4, DLA-EABA, OFRCNN, NeuroPET and O-IBGC-BiLSTM-ISSA classifiers. Notably, O-IBGC-BiLSTM-ISSA emerges as a standout method for achieving highly

accurate predictions, boasting an impressive accuracy rate of 96.51%. Comparatively, prior methods such as YOLO-V4, DLA-EABA, OFRCNN and NeuroPET yield accuracy rates of 91%, 80%, 92.6040% and 95.02% respectively. The high accuracy achieved by the O-IBGC-BiLSTM-ISSA framework, trained for BC classification in PET images, followed by the hyperparameter tunning of deep learning network using ISSA, can be attributed to its holistic approach and several key components.

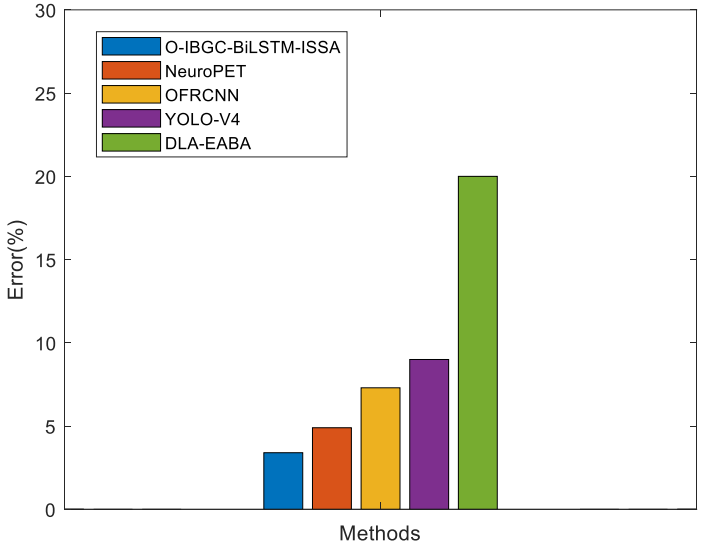

Figure 9: Scalability evaluation of the suggested model and benchmark models by Error Rate

The graph depicted in Figure 9 showcases the comparison of error rates for attack detection using methods including YOLO-V4, DLA-EABA, OFRCNN, NeuroPET and O-IBGC-BiLSTM-ISSA classifiers. It is evident that the proposed O-IBGC-BiLSTM-ISSA attains low error rate of 3.4, indicating its efficiency in processing detections swiftly.

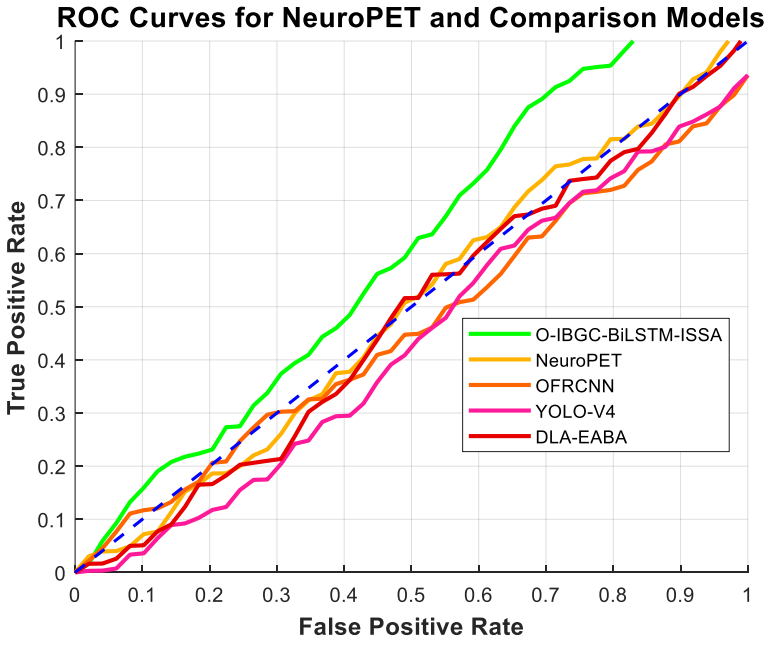

Figure 10: ROC curve

Figure 10 compares the ROC curves of O-IBGC-BiLSTM-ISSA with the comparison models (YOLO-V4, DLA-EABA, OFRCNN and NeuroPET). For various decision thresholds, this graph compares the FP Rate (FPR = 1-Specificity (SP)) against the TP Rate (TPR or Sensitivity (S)). It shows the way the framework effectively distinguishes between the positive (cancer) and negative (no cancer) classes over a range of threshold settings. The AUC is a summary metric of the ROC curve. The model's overall accuracy in effectively ranking positive samples higher than negative ones is indicated by a higher AUC score.

According to the figure 11, O-IBGC-BiLSTM-ISSA demonstrates a superior AUC compared to the other models (NeuroPET, OFRCNN, DLA-EABA, and YOLO-V4). This means that across all possible thresholds, O-IBGC-BiLSTM-ISSA strikes a better balance between S (accurately eliminating cancer cases) and specificity (accurately eliminating non-cancer cases).

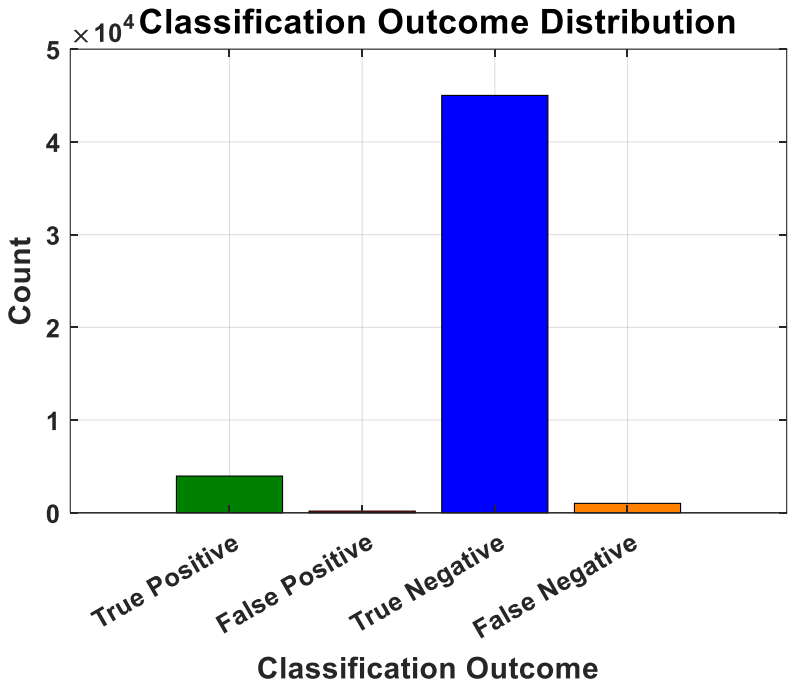

Figure 11: Cancer classification graph for TP, FP, TN, and FN

Figure 11 visually displays the counts of TPs, FPs, TNs, and FNs, giving a quick snapshot of the classification outcomes. This graph visually displays the values:
(TP = 3,962): Cases where the model correctly identifies the presence of cancer.
(FP = 101): Cases where the model incorrectly predicts cancer in non-cancer cases. Although a low FP count is generally positive, false positives can lead to unnecessary further testing or anxiety.
(TN = 45,016): Cases where the model correctly identifies the absence of cancer.
(FN = 1,097): Cases where the model fails to detect cancer even though it is present. This is a critical issue in medical diagnosis because missing a cancer diagnosis can have severe consequences. The figure 11 shows the reveals that even a model with excellent overall discrimination can have areas needing improvement—specifically, the relatively high false negative rate (FN = 2,022) which is a critical concern in cancer detection.

5. CONCLUSION AND FUTURE WORK

In this study, we propose a comprehensive framework for BCD in PET images by integrating advanced techniques to improve accuracy and robustness. The framework includes noise removal using the Hyper-Averaging Filter (HAF), segmentation with the Improved BIRCH algorithm, feature extraction with Gray-level zone length matrix (GLZLM), and feature selection using the mRMR method. For classification, we introduce a novel hybrid model, O-IBGC-BiLSTM, which combines Graph Convolutional Networks (GCNs) and Bidirectional LSTM (BiLSTM) units. The framework's efficiency is further enhanced by hyperparameter tuning through the Improved Sparrow Search Algorithm (ISSA). Evaluation using the QIN-Breast dataset shows that the proposed framework is effective in accurate BCD, offering a robust solution for early diagnosis and better treatment planning. The suggested O-IBGC-BiLSTM-ISSA method achieving highly accurate predictions, boasting an impressive accuracy rate of 96.51%. The future it may be possible to improve the model's capacity to recognize intricate patterns in PET images by investigating further advanced feature extraction techniques, such as deep learning-based feature extraction using convolutional neural networks (CNNs).

While the proposed O-IBGC-BiLSTM-ISSA framework has demonstrated high accuracy (96.51%) in detecting breast cancer in PET images, several potential areas for future improvement and expansion remain:

1. Advanced FE Techniques
   - Integrating DL-based FE using CNN can further enhance the ability to recognize complex patterns in PET images.
   - Exploring transformer-based architectures, such as Vision Transformers (ViTs), may improve the model's contextual understanding of PET images.
2. Multi-Modal Data Fusion
   - Combining PET images with other imaging modalities, such as MRI or CT scans, can provide a more comprehensive assessment of breast cancer.
   - Incorporating radiomics features from multimodal data can improve the robustness of the classification process.
3. Enhanced Segmentation Methods
   - Exploring DL-based segmentation methods, such as U-Net or Mask R-CNN, could refine lesion detection and segmentation.
   - Adopting self-supervised or semi-supervised learning approaches may help handle cases with limited labeled data.

References

1. Abunasser B.S., Daud S.M., Zaqout I.S., Abu-Naser S.S. Convolution neural network for breast cancer detection and classification–final results, Journal of Theoretical and Applied Information Technology, 101 (1) (2023).
2. Wang Z., Li M., Wang H., Jiang H., Yao Y., Zhang H., Xin J. Breast cancer detection using extreme learning machine based on feature fusion with CNN deep features, IEEE Access, 7 (2019), pp. 105146-105158.
3. Jafari, Z., & Karami, E. (2023). Breast cancer detection in mammography images: A CNN-based approach with feature selection. Information, 14(7), 410.
4. Bray, F., Laversanne, M., Sung, H., Ferlay, J., Siegel, R. L., Soerjomataram, I., & Jemal, A. (2024). Global cancer statistics 2022: GLOBOCAN estimates of incidence and mortality worldwide for 36 cancers in 185 countries. CA: a cancer journal for clinicians, 74(3), 229-263.
5. Bilal, A., Imran, A., Baig, T.I. et al. Breast cancer diagnosis using support vector machine optimized by improved quantum inspired grey wolf optimization. Sci Rep 14, 10714 (2024). https://doi.org/10.1038/s41598-024-61322-w
6. Umer M.J., Sharif M., Kadry S., Alharbi A. Multi-class classification of breast cancer using 6B-net with deep feature fusion and selection method, Journal of Personalized Medicine, 12 (5) (2022), p. 683
7. Tan Y., Sim K., Ting F., Breast cancer detection using convolutional neural networks for mammogram imaging system, 2017 international conference on robotics, automation and sciences, IEEE (2017), pp. 1-5
8. Essa, H.A., Ismaiel, E. & Hinnawi, M.F.A. Feature-based detection of breast cancer using convolutional neural network and feature engineering. Sci Rep 14, 22215 (2024). https://doi.org/10.1038/s41598-024-73083-7
9. Abunasser B.S., AL-Hiealy M.R.J., Zaqout I.S., Abu-Naser S.S., Breast cancer detection and classification using deep learning xception algorithm, International Journal of Advanced Computer Science and Applications, 13 (7) (2022)
10. Sushanki, S., Bhandari, A. K. & Singh, A. K. A review of computational methods for breast cancer detection in ultrasound images using multi-image modalities. Archives of Computational Methods in Engineering 31(3), 1277–1296 (2024).
11. Abdullakutty, F., Akbari, Y., Al-Maadeed, S., Bouridane, A. and Hamoudi, R., 2024. Advancing Histopathology-Based Breast Cancer Diagnosis: Insights into Multi-Modality and Explainability. arXiv preprint arXiv:2406.12897.
12. Oyelade, O. N., Irunokhai, E. A. & Wang, H. A twin convolutional neural network with a hybrid binary optimizer for multi-modal breast cancer digital image classification. Scientific Reports 14(1), 692 (2024).
13. Hu, H., Liang, W., Zou, X. and Zou, X., 2024, July. Graph Convolutional Networks Based Multi-modal Data Integration for Breast Cancer Survival Prediction. In International Conference on Intelligent Computing (pp. 85–98). Singapore: Springer Nature Singapore.
14. Imokawa, T., Satoh, Y., Fujioka, T., Takahashi, K., Mori, M., Kubota, K., ... & Tateishi, U. (2023). Deep learning model with collage images for the segmentation of dedicated breast positron emission tomography images. Breast Cancer, 1-8.
15. Tsukijima, M., Teramoto, A., Kojima, A., Yamamuro, O., Tamaki, T., & Fujita, H. (2023). A position-adaptive noise-reduction method using a deep denoising filter bank for dedicated breast positron emission tomography images. Physical and Engineering Sciences in Medicine, 1-13.
16. Sueoka, S., Sasada, S., Masumoto, N., Emi, A., Kadoya, T., & Okada, M. (2021). Performance of dedicated breast positron emission tomography in the detection of small and low-grade breast cancer. Breast Cancer Research and Treatment, 187, 125-133.
17. Chen, X., Zhang, Z., & Zhang, L. (2017). Image filtering and enhancement techniques for medical image processing. IEEE Access, 5, 19303-19311.
18. Fan, J., & Liu, H. (2018). A Modified BIRCH Algorithm for Image Segmentation in Medical Diagnosis. International Journal of Computational Intelligence Systems, 11(2), 482-492.

19. Liu, Z., & Xing, F. (2016). Radiomics for Predicting Clinical Outcomes of Cancer Patients: A Systematic Review and Meta-Analysis. Journal of Medical Imaging, 3(4), 413-421.
20. Zhang, Y., et al. (2019). Comparison of Machine Learning Approaches for Predicting the Recurrence of Breast Cancer Using PET Radiomics. IEEE Transactions on Medical Imaging, 38(12), 2774-2781.
21. Shin, H. C., et al. (2016). Deep Convolutional Neural Networks for Computer-Aided Detection: CNN Architectures, Dataset Characteristics, and Transfer Learning. IEEE Transactions on Medical Imaging, 35(5), 1285-1298.
22. Fallahpoor, M., Chakraborty, S., Pradhan, B., Faust, O., Barua, P. D., Chegeni, H., & Acharya, R. (2024). Deep learning techniques in PET/CT imaging: A comprehensive review from sinogram to image space. Computer methods and programs in biomedicine, 243, 107880.
23. Dalal, S., Jaglan, V., Agrawal, A., Kumar, A., Joshi, S. J., & Dahiya, M. (2024, December). Navigating urban congestion: Optimizing LSTM with RNN in traffic prediction. In AIP Conference Proceedings (Vol. 3217, No. 1). AIP Publishing.
24. Xiang, Y. (2025, February). Optimizing Stock Trend Prediction in the Chinese Market: A Comparative Study of Machine Learning Models with Bayesian Hyperparameter Tuning. In International Workshop on Navigating the Digital Business Frontier for Sustainable Financial Innovation (ICDEBA 2024) (pp. 599-614). Atlantis Press.
25. Yue, Y., Cao, L., Lu, D., Hu, Z., Xu, M., Wang, S., ... & Ding, H. (2023). Review and empirical analysis of sparrow search algorithm. Artificial Intelligence Review, 56(10), 10867-10919.
26. Hong, C., Liang, Q., Liang, Q., Yu, W., Yu, W., & Xiong, N. (2024). Sparrow Search Algorithm with Adaptive Collaborative Updating.
27. Hamed, G., Marey, M., Amin, S. E., & Tolba, M. F. (2021). Automated Breast Cancer Detection and Classification in Full Field Digital Mammograms Using Two Full and Cropped Detection Paths Approach. IEEE Access, 9, 116898-116913.
28. Zheng, J., Lin, D., Gao, Z., Wang, S., He, M., & Fan, J. (2020). Deep learning assisted efficient AdaBoost algorithm for breast cancer detection and early diagnosis. IEEE Access, 8, 96946-96954.